

Comparison of four kernel functions used in support vector machines for landslide susceptibility mapping: a case study at Suichuan area (China)

Haoyuan Hong, Biswajeet Pradhan, Dieu Tien Bui, Chong Xu, Ahmed M. Youssef & Wei Chen

To cite this article: Haoyuan Hong, Biswajeet Pradhan, Dieu Tien Bui, Chong Xu, Ahmed M. Youssef & Wei Chen (2017) Comparison of four kernel functions used in support vector machines for landslide susceptibility mapping: a case study at Suichuan area (China), *Geomatics, Natural Hazards and Risk*, 8:2, 544-569, DOI: [10.1080/19475705.2016.1250112](https://doi.org/10.1080/19475705.2016.1250112)

To link to this article: <https://doi.org/10.1080/19475705.2016.1250112>



© 2016 The Author(s). Published by Informa UK Limited, trading as Taylor & Francis Group



Published online: 17 Nov 2016.



[Submit your article to this journal](#)



Article views: 588



[View related articles](#)



[View Crossmark data](#)



Citing articles: 5 [View citing articles](#)



Comparison of four kernel functions used in support vector machines for landslide susceptibility mapping: a case study at Suichuan area (China)

Haoyuan Hong ^{a,b}, Biswajeet Pradhan ^{c,d}, Dieu Tien Bui ^e, Chong Xu ^a, Ahmed M. Youssef^f and Wei Chen ^g

^aKey Laboratory of Active Tectonics and Volcano, Institute of Geology, China Earthquake Administration, Beijing, P.R. China; ^bJiangxi Provincial Meteorological Observatory, Jiangxi Meteorological Bureau, Nanchang, China; ^cDepartment of Civil Engineering, Geospatial Information Science Research Center (GISRC), Faculty of Engineering, University Putra Malaysia, Selangor Darul Ehsan, Malaysia; ^dDepartment of Energy and Mineral Resources Engineering, Choongmu-gwan, Sejong University, Seoul, Republic of Korea; ^eGeographic Information System group, Department of Business Administration and Computer Science, University College of Southeast Norway, Bø i Telemark, Norway; ^fDepartment of Geology, Faculty of Science, Sohag University, Sohag, Egypt; ^gCollege of Geology & Environment, Xi'an University of Science and Technology, Xi'an, China

ABSTRACT

Suichuan is a mountainous area at the Jiangxi province in Central China, where rainfall-induced landslides occur frequently. The purpose of this study is to assess landslide susceptibility of this region using support vector machine (SVM) with four kernel functions: polynomial (PL), radial basis function (RBF), sigmoid (SIG), and linear (LN). A total of 178 landslides were used to accomplish this approach, of which, 125 (70%) landslides were randomly selected for training the landslide susceptibility models, whereas the remaining 53 (30%) were used for the model validation. Fifteen landslide conditioning factors were considered including slope-angle, altitude, slope-aspect, topographic wetness index (TWI), sediment transport index (STI), stream power index (SPI), plan curvature, profile curvature, distance to rivers, distance to faults, distance to roads, precipitation, landuse, normalized difference vegetation index (NDVI), and lithology. Using the training dataset, nine landslide susceptibility models for the Suichuan area were constructed with the four kernel functions. To evaluate the performance of these models, the receiver-operating characteristic curve (ROC) and area under the curve (AUC) were used. Using the training dataset, AUC values for the SVM-PL models with six degrees PL function (1–6) are 0.715, 0.801, 0.856, 0.891, 0.919, 0.953, respectively, and for the SVM-RBF model, the SVM-SIG model, and the SVM-LN model are 0.716, 0.741, and 0.740, respectively. Using the validation dataset, AUC values for the SVM-PL models with six degrees PL function (1–6) are 0.738, 0.730, 0.683, 0.648, 0.608, and 0.598, respectively, and for the SVM-RBF model, the SVM-SIG model, and the SVM-LN model are 0.716, 0.741, and 0.740, respectively. Our results suggested that the SVM-RBF model is the most suitable for landslide susceptibility assessment for the study area.

ARTICLE HISTORY

Received 11 March 2016
Accepted 10 October 2016

KEYWORDS

Support vector machines; GIS; landslide; remote sensing; Suichuan; China

1. Introduction

In mountainous regions, landslides are considered as the most costly and damaging natural hazards that cause thousands of deaths every year and losses of billions of dollars (Michel et al. 2014). Landslides occur as results of complicated and perplexed processes (Feuillet et al. 2014; Perrone et al. 2014), and in general, earthquake and rainfall are considered as the two major triggering (Ding et al. 2014; West et al. 2014). To reduce the serious consequences induced by landslides, in recent years, many scientists have been engaged in landslide susceptibility mapping, and consequently, various methods and techniques have been exploited (Carey & Petley 2014; Hassaballa et al. 2014; Lissak et al. 2014). These methods and techniques were established in combining with Geographic Information System (GIS) and remote sensing (RS), and in general, process of producing landslide susceptibility maps is more easier and accurate (Klose et al. 2014; Paulín et al. 2014).

Although many models have been proposed for landslide susceptibility mapping, until now most scholars have different opinions about the models selection, some of them try to contrast the models to acquire a result in a study area; this may be a good way to compare the advantages and disadvantages of each model (Yalcin et al. 2011; Pourghasemi et al. 2012a; Kavzoglu et al. 2014; Umar et al. 2014; Youssef et al. 2014, 2015). Several models were conducted to produce landslide susceptibility map including logistic regression (Ercanoglu & Temiz 2011; Akgun 2012; Conoscenti et al. 2014; Kavzoglu et al. 2014), artificial neural network (Li et al. 2014), support vector machine (SVM) (Chen et al. 2016a; Hong et al. 2015, 2016; Li and Kong 2014; Peng et al. 2014), decision tree (Yeon et al. 2010; Pradhan, 2011; Alkhasawneh et al. 2014), evidential belief functions (Althuwaynee et al. 2012; Pradhan, *et al.* 2014), index of entropy (Constantin et al. 2011; Pourghasemi et al. 2012b), weights of evidence (Chen et al. 2016b; Neuhaeuser et al. 2012; Tehrany et al. 2014), analytical hierarchy process (Chen et al. 2016c; Shahabi et al. 2014), and frequency ratio (Pradhan and Lee, 2010; Demir et al. 2013). Among all these methods, the SVM model is new technique in landslide susceptibility mapping and it becomes more and more popular, due to its procedure is based on soft computing statistical theory (Yilmaz et al. 2010; Xu et al. 2012).

China is the most populous country worldwide, thousands of years of human activity, the history of the endless wars, especially in recent decades the rapid development of economy and population growth rate, but also the use of the nature resources has been increased leading to a strong interfere with the natural environment (Huang et al., 2014; Miao et al., 2014). In the eastern and central regions of China, due to the large number of extraction of groundwater and massive exploitation of mineral resources (including oil and gas resources), resulting in the destruction of groundwater resources and geotechnical equilibrium state of tectonic stress changes induced and exacerbated land subsidence, ground subsidence, ground fissures, land salinization, swamping, development and hazards of geological disasters collapse, slip, flow, mine disasters (Dong et al. 2014; Xu & Xu 2014a; 2014b; Xu et al., 2013a, 2013b).

In the western region of China, due to the development and other over-development of land, grasslands, forests and water resources, different problems were raised, including acceleration of soil erosion, desertification and contain collapse, landslides, and mudslides (Yin, 2014). Landslides have caused huge economic losses and casualties every year. Therefore, prevention and control of landslide disasters for China have a special significance (Zhao et al. 2014; Zhuang et al. 2014). In summary, landslides susceptibility mapping become more and more important in landuse planning and government management all over the world (Coe 2012; Moretti et al. 2012)

The aim of this study is to produce landslide susceptibility maps using SVM model in the Sichuan area of China. The major achieve of this study is to contrast the results between four kernel functions named polynomial (PL), Lineal, Radial basis, and SIG. Besides, in PL, six kinds of degree from 1 to 6 were applied to verify the accuracy of the kernel functions. Finally, nine landslide susceptibility maps using four kernel functions in SVM model were produced.

2. Study area and data used

2.1. Study area

The Suichuan area is located in the southern section of Luoxiao Mountain, the southwest border of Jiangxi Province of China. The study area lies between latitudes 25° 28' 32" N. and 26° 42' 55" N., and longitudes 113° 56' 51" E. and 114° 45' 45" E. It covers an area of 3,144 km². Suichuan area is from the southwest to the northeast of Wanyang mountain; there are low mountains, hills and river valley plain. The county has two major rivers, Shu River, is a tributary of Ganjiang river (<http://www.jxyh.gov.cn>).

Suichuan area belongs to the subtropical monsoon climate, the annual precipitation ranges from 1,111.2 mm to 2241.3 mm with an average of ~1,653 mm. The rainy season falls within March to September, accounting for 77.6% of the yearly rain, according to meteorological data (1960–2012 year) of Suichuan area (<http://www.weather.org.cn>). The area is characterized by an average annual temperature of ~18.6 °C and average annual sunshine 1720.3 hours. In the Suichuan area, there was no information about earthquake-induced landslides and about the high amount of precipitation that induced landslides. Figure 1 shows the landslide location and some recent photo about landslide disaster.

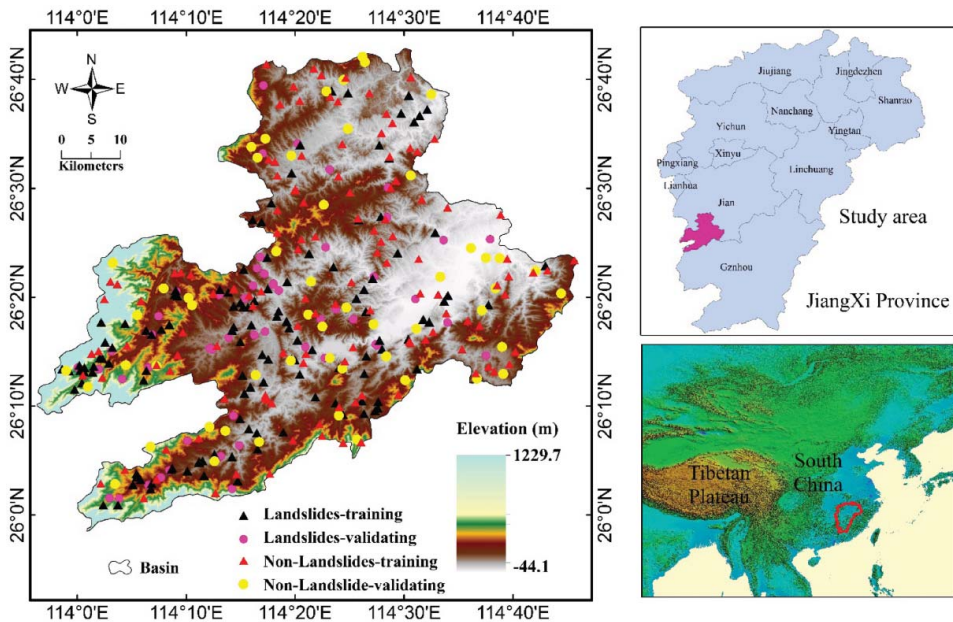


Figure 1. Landslide location map of the study area.

Table 1. Types of geological formation of the study area.

No.	Unit name	Lithology	Geological age
A	Zi Shan Group	Grey sandstone siltstone shale carbonaceous shale and coal seam clamp	Carboniferous
B	Xiashan group, Luo soil group, Xiashan group, Yunshan formation shed group	Grey quartz conglomerate pebbly sandstone; purple red sandstone siltstone silty rocks interbedded with grey green sandstone shale dolomite dark grey dolomitic limestone	Devonian
	Mashan Group, Yang Lake Group	Grey calcareous mudstone siltstone interbedded with limestone; limestone clip purple sand siltstone silty shale chamosite sandstone olitic hematite	Devonian
C	The forest group, North Water Group	Grey white feldspar quartz sandstone pebbly sandstone fine sandstone siltstone interbedded with sandy shale carbonaceous shale and coal seam	Jurassic
		The upper part of purple yellow green sandstone siltstone interbedded with shales the lower part of purple pebbly sandstone fine sandstone conglomerate monzonitic granite	Jurassic
	Changle street, Sanjiang port Guposhan, Xishan, Da Zhen Copper, Ling super unit		Jurassic
	Moon shape goose shape, Lingshan super unit	monzonitic granite	Jurassic
	Jiuxian decoction Mufu mountain, Changshan match, Yangguan super unit, Huang XieXihua mountain super unit	monzonitic granite	Jurassic
	Huang Xie the sea will be under the Xihua mountain, Changshan super unit	monzonitic granite	Jurassic
D	Xin Wei super unit, new around the unit, Yunju mountain super unit	Brick red purple red conglomerate pebbly sandstone sandstone mudstone and silt the bottom conglomerate	Cretaceous
	Gui Feng Group, Lotus pond river group,	Purplish red brick red sandstone intercalated with sandstone the lower clamp andesitic tuff calcium mirabilite Shi Yan lding Xuan takeiwa	Cretaceous
E	The Aoto group, Grand Valley Group	Yellow green sandstone fine sandstone and silty slate slate black carbonaceous siliceous slate and shale interbed	Ordovician
	The otolith group, Shi Kou group	The otolith group (upper) Shi Kou group (middle lower)	Ordovician
F	-	Water	Quaternary -
G	The waterwheel Guidong snow top super unit	monzonitic granite	Silurian
	The Zuo An chao estuary Nanping Hill unit, large clutch unit	granodiorite	Silurian
	Tang Hu chao unit, Fu Fang chao car brain unit, high delta unit	Tonalite diorite porphyritic granodiorite granite porphyritic two porphyritic moyite	Silurian
	Fu Fangchao unit, Gaoping unit, cat nasal Yin unit	monzonitic granite	Silurian
H	The urban super unit, Qing xi over unit, Qiaotou super unit, jade Jing shan super unit	biotitemonzonitic granite	Triassic
I	Le chang xia Group	Grey purple feldspar quartz sandstone intercalated with siltstone slate; light grey chert sandwiched phyllite	Upper Sinian
J	Eight village group high group	Grey greyish green sandstones with grey green silty slate slate and a small amount of carbonaceous slate	Cambrian
	Eight village Stone Group	Grey green striped strip slate with metaclastics bottom common lenticular limestone	Cambrian

Note: *A B C D E F G H I J represent the class of lithology.

The altitude of the area ranges from -44.6 to 1229.7 m above sea level. Around 33.6% of the study area has a slope gradient less than 15° whereas areas with a slope gradient larger than 30° account for 13.6% of the total study area. Areas fall into the slope category $15^\circ-30^\circ$ account for 52.8% of the total study area.

The geological structure of Suichuan area is complex. More than 48 geological groups and units are recognized (Table 1). The main lithological units in the study area are limestone, sandstone, silty slate, carbonaceous slate (Figure 2).

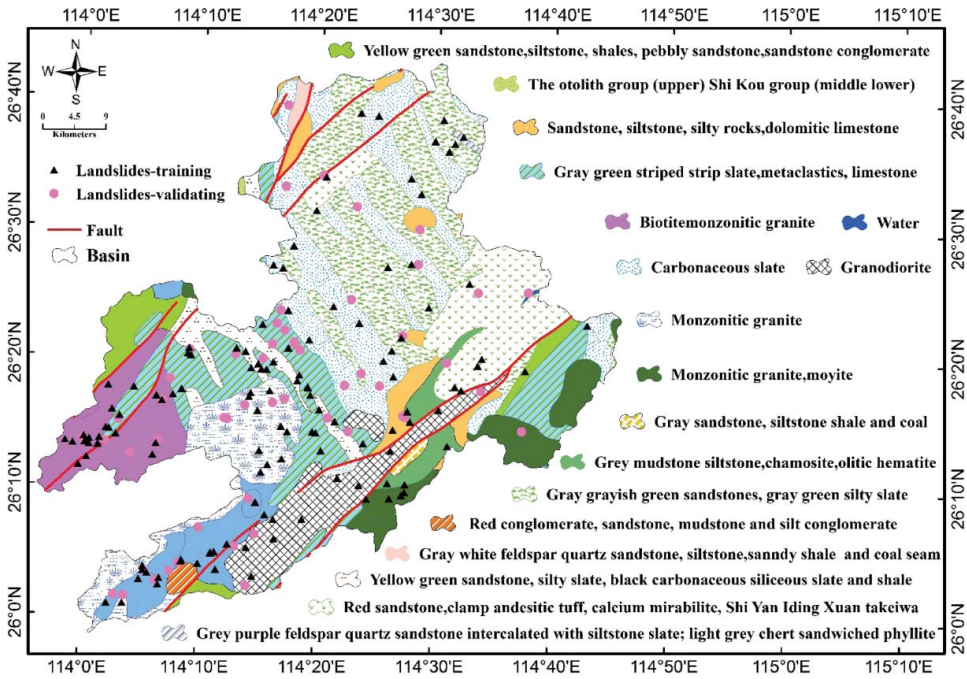


Figure 2. Geologic map of the study area.

2.2. Data

2.2.1. Landslide inventory map

Landslide inventory map is the important step in landslide susceptibility assessment and the map can be constructed using various methods such as field survey, satellite image interpretation, aerial photograph, historical records (Pham et al. 2015). In this study, a landslide inventory map with 178 landslide events was established and these landslides were determined from interpretations of high resolution satellite images at the Google Earth®, historical records, and field surveys.

Our analysis of these landslide shows that the size of the smallest landslide is 12 m², the largest is 45,000 m², and the average is 2,508.5 m². The landslide inventory map consists of 104 rotational slides and 74 translational slides, besides 84 slides are shallow and 94 are deep. Larger landslides (>800 m²) account for around 5.8% of the total number of landslides. These landslides have been reported affecting 1,987 people. Around 27.7% of the total landslides are medium size (200–800 m²) and affected 1,134 people. Small-sized landslides (<200 m²) that affected 985 people are accounted for 66.5% of the total landslides.

2.2.2. Landslide predisposing factors

The landslide predisposing factors are very complex, until now there is no agreement with the total and deep cause of landslide. However, in most literatures, scientists study the relationship between landslide occurrence with conditioning factor such as topographical, geological, and climatic conditions. Based on literature review and analysis characteristics of the landslide inventory map of the Suichuan area, 15 factors were selected. They are slope-angle, altitude, slope-aspect, topographic wetness index (TWI), sediment transport index (STI), stream power index (SPI), plan curvature, profile curvature, distance to rivers, distance to faults, distance to roads, precipitation, landuse, normalized difference vegetation index (NDVI), and lithology were considered as major factors to produce landslide susceptibility map of the study area.

2.2.3. Digital elevation model and derivatives

A digital elevation model (DEM) for the study area with a spatial resolution of 25×25 m was generated from topographic maps. DEM of the study area was used to extract different conditioning factors such as slope-angle, altitude, slope-aspect, TWI, STI, SPI, plan curvature, and profile curvature. Slope-angle is a quantitative description of the extent of ground tilt, but also a basic landform index, through the influence of gravity, surface runoff and soil erosion affect the occurrence and intensity of erosion. For medium-sized basin and regional scale distributed hydrological and soil erosion model, the slope-angle of the surface is the most basic model parameters (Pedrazzini et al. 2013; Muceku and Korini 2014). The slope-angle map was prepared from the DEM, and reclassified into four categories: (1) $0-5^\circ$, (2) $5-15^\circ$, (3) $15-30^\circ$, (4) $>30^\circ$ (Figure 3a). Altitude was classified to five categories including <200 m, $200-400$ m, $400-600$ m, $600-800$ m, and >800 m (Figure 3b). The slope-aspect (Figure 3c) values are grouped into nine classes based on normal or common standard classification, including flat (-1°), north ($337.5^\circ-360^\circ$ and $0^\circ-22.5^\circ$), northeast ($22.5^\circ-67.5^\circ$), east ($67.5^\circ-112.5^\circ$), southeast ($112.5^\circ-157.5^\circ$), south ($157.5^\circ-202.5^\circ$), southwest ($202.5^\circ-247.5^\circ$), west ($247.5^\circ-292.5^\circ$), and northwest ($292.5^\circ-337.5^\circ$). TWI is a kind of stream length through quantitative description of runoff area, but also the watershed soil moisture and runoff generation capacity. It is defined as

$$TWI = \ln \left(\frac{\alpha}{\tan \beta} \right), \quad (1)$$

where α is the cumulative upslope area draining through a point (per unit contour length), and $\tan \beta$ is the slope-angle at the point. It reflects the tendency of water to accumulate at any point in the catchment (in terms of α) and the tendency of gravitational forces to move that water down slope (expressed in terms of $\tan \beta$ as an approximate hydraulic gradient) (Moore & Grayson 1991; Poudyal et al. 2010). In the present study, TWI is divided into three classes <7 , $7-11$, and >11 (Figure 3d). STI represents potential of soil loss from the combined slope properties (Figure 3e). This index is derived from unit stream-power theory and is sometimes used in place of the length-slope factor in the revised universal soil loss equation (RUSLE) for slope lengths less than 100 m and slope less than 14° . STI depends on two parameters A_s (is the upslope contributing area) and β (is the local slope gradient in degrees). In the current study, the STI factor was classified into three categories, including <10 , $10-30$, and >30 and was prepared according to the following equation:

$$STI = \left(\frac{A_s}{22.13} \right)^{0.6} \times \left(\frac{\sin \beta}{0.0896} \right)^{1.3} \quad (2)$$

The SPI is a factor that measures the erosive power of flowing water based on the assumption that discharge is proportional to specific catchment area (Moore & Grayson 1991). The SPI depends on two parameters. The SPI (Figure 3f) can be defined as (Moore & Grayson 1991) as

$$SPI = A_s \tan(\beta) \quad (3)$$

where A_s is the specific catchment area and β is the local slope gradient measured in degrees. In the current study, SPI was reclassified into five categories such as <20 , $20-40$, $40-60$, $60-80$, and >80 .

Plan curvature reflects the structure and morphology of the terrain, but also affects the distribution of soil organic matter content in the surface process simulation and hydrology, soil areas has important implications (Hapke and Green, 2006). Profile curvature is a measure of the slope gradient of the ground along the direction of the rate of change in ground elevation of maximum gradient (May et al. 2013). In the current study, plan curvature (Figure 3g) was divided into three categories

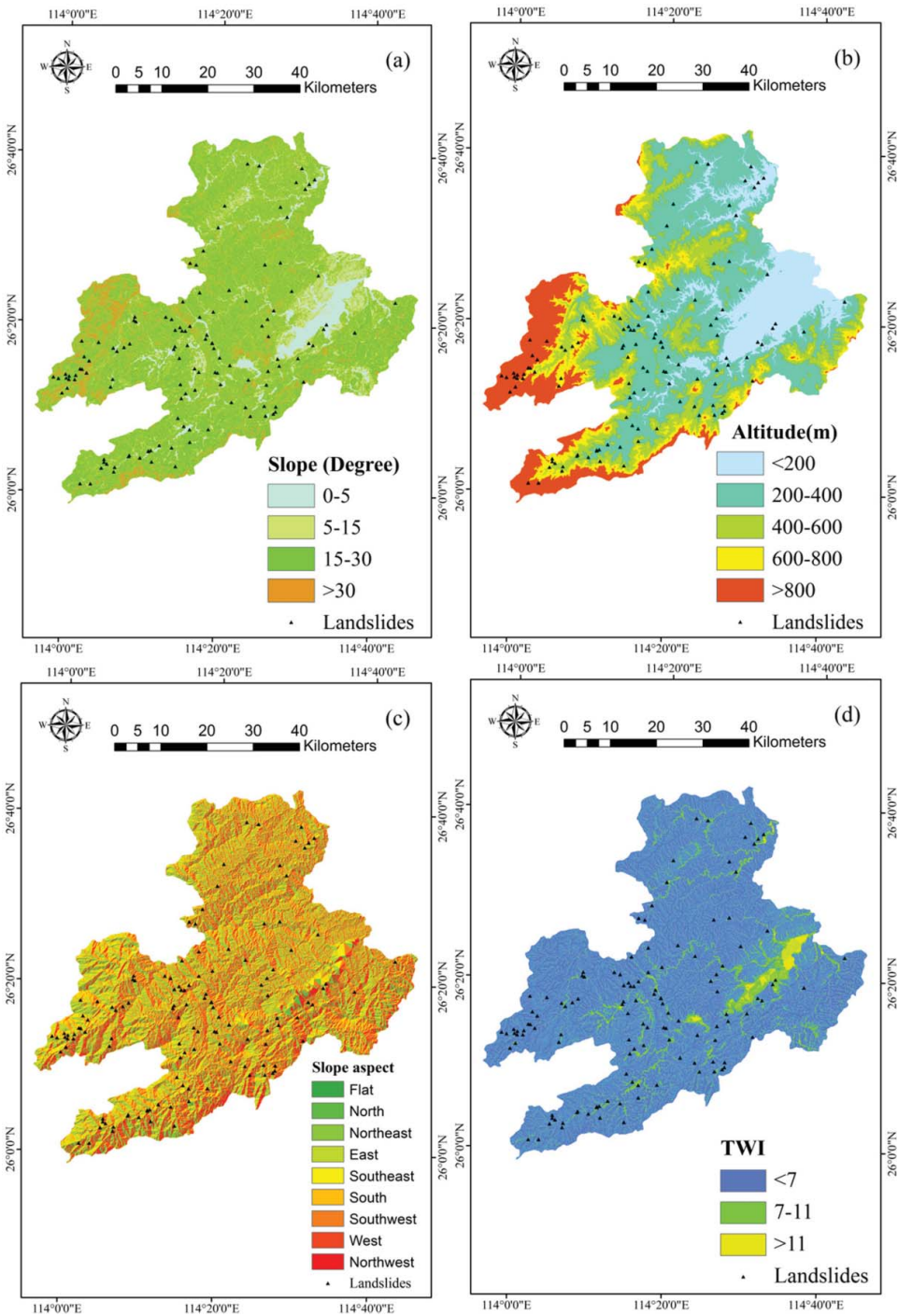


Figure 3. Topographical parameter maps of the study area: (a) slope-angle, (b) altitude, (c) slope-aspect, (d) topographic wetness index (TWI), (e) sediment transport index (STI), (f) stream power index (SPI), (g) plan curvature, and (h) profile curvature.

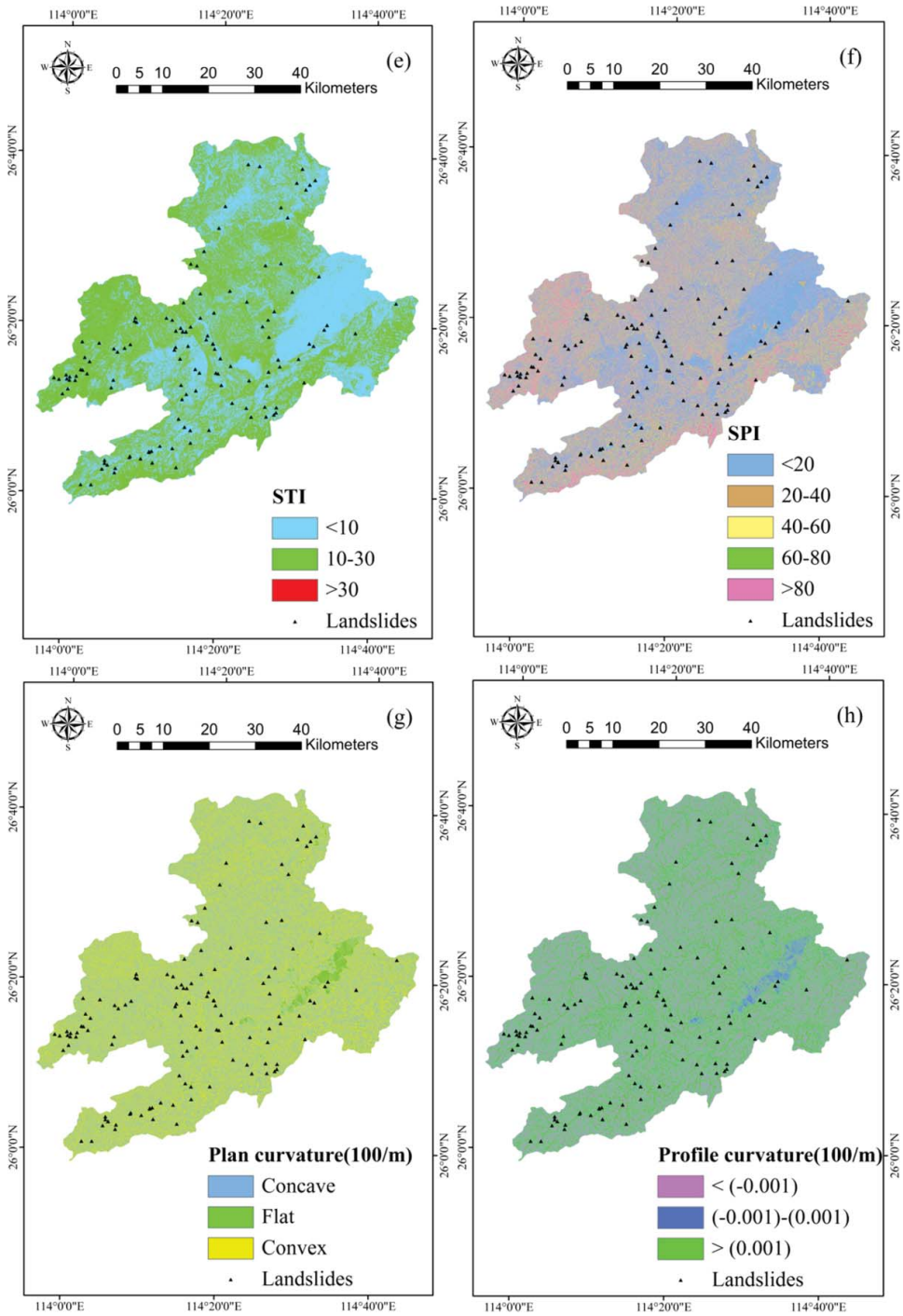


Figure 3. (Continued).

including: concave, flat, and convex. Profile curvature (Figure 3h) was ranged from <-0.001 , -0.001 to 0.001 , and >0.001 .

2.2.4. Distance to rivers, distance to faults, and distance to roads

Some authors found that faults could induce zones of weakness (reduced bulk-rock strength) that increase hillslope susceptibility to failure (Klose et al. 2014; Paulín et al. 2014). In addition, an extensive landsliding in response to a large outburst flood indicates that lateral river erosion is a key driver of landslide erosion on threshold hillslopes, the fault and river become key factors causing landslide (Weng et al. 2011; Scheingross et al. 2013). The river network that undercut slopes was extracted from the topographic map (scale 1:50000) by buffering the river lines. The rivers buffer map was classified into five categories including $<100\text{m}$, $100\text{--}300\text{m}$, $300\text{--}500\text{m}$, $500\text{--}700\text{m}$, and $>700\text{m}$ (Figure 4a). However, the distance to fault map was constructed by buffering the fault lines and classified into five categories $<500\text{m}$, $500\text{--}1000\text{m}$, $1000\text{--}2000\text{m}$, $2000\text{--}3000\text{m}$, $>3000\text{m}$ (Figure 4b). The distance to roads is an important factor of landslides. Many landslides occur along the roads because of uncontrolled rock cuts. Highways and roads construction can cause slope disturbance causing increase of the strain behind the slope and leading to development of some tension cracks. In the current study, many landslides were recorded along the roads. The distance to roads map was prepared by buffering the road lines and classified into five categories including $<500\text{m}$, $500\text{--}1,000\text{m}$, $1,000\text{--}2,000\text{m}$, $2,000\text{--}3,000\text{m}$, and $>3,000\text{m}$ (Figure 4c).

2.2.5. Precipitation

Precipitation is one of the most major triggered factors of landslides. It had been paid more attention by many scientists (Raia et al. 2013). The precipitation data were extracted from a database from the government of Jiangxi Province Meteorological Bureau. The mean annual precipitation for

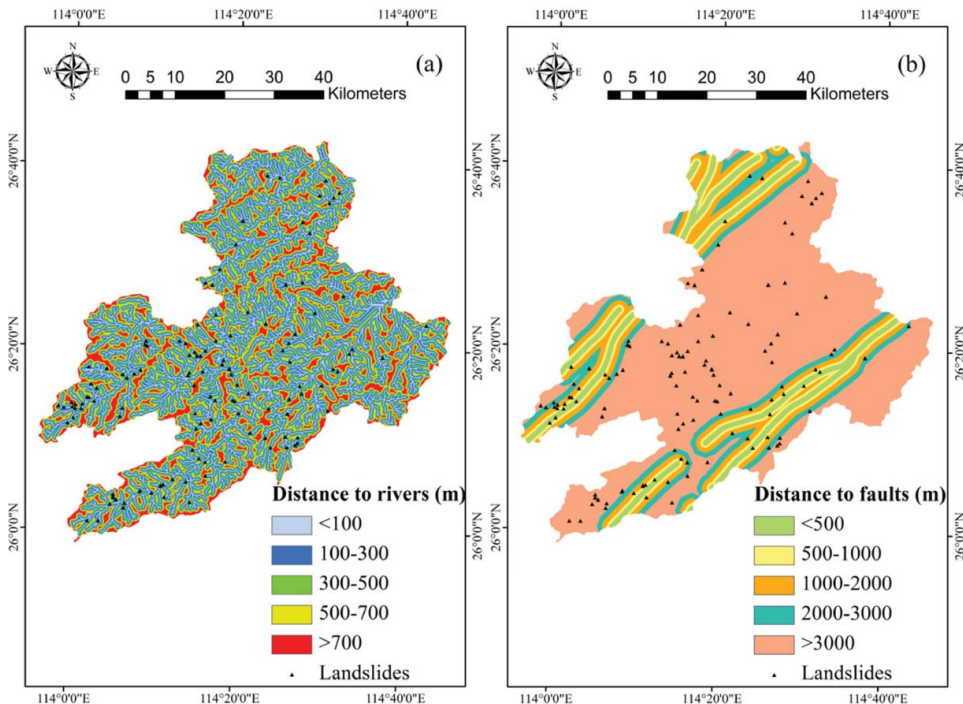


Figure 4. Other conditioning factors maps including: (a) distance to river, (b) distance to fault, (c) distance to roads, (d) precipitation, (e) land use, and (f) NDVI.

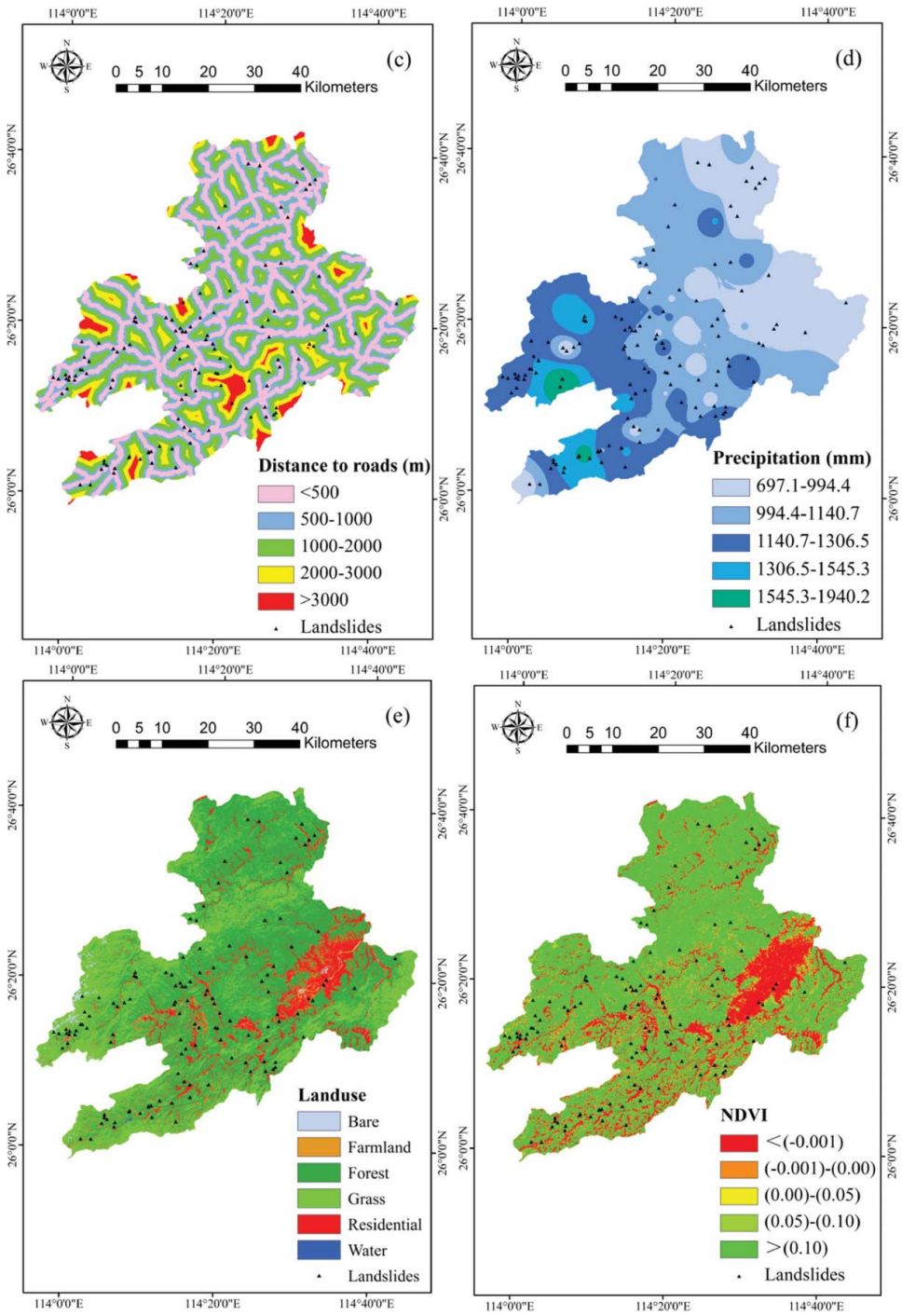


Figure 4. (Continued).

the period 1960–2014 at 23 weather stations was used to draw the rainfall map using Kriging method. The precipitation map was classified into five divisions including 697.1–994.4 mm, 994.4–1140.7 mm, 1140.7–1306.5 mm, 1306.5–1545.3 mm, and 1545.3–1940.2 mm for the study area (Figure 4d).

2.2.6. Landuse

Landuse has some relationship with the landslide, they are influenced each other, where unreasonable mining and building may induced landslide (Hadmoko et al. 2010). With ENVI software, the role of landuse distribution in landslide susceptibility was evaluated by applying Maximum likelihood classification method to Landsat 7 ETM+ satellite image (acquired in 1999.12.10). Maximum likelihood generated high accuracy results (Kappa coefficient = 0.924) by taking a set of input data (Suichuan area). The landuse map in the study area was divided into six classes (Figure 4e), namely, water, residential area, forest, bare, farmland, and grass. The forest unit represents the maximum percentage (about 58.9%) of the landuse map, whereas the water unit represents the minimum percentage (about 0.02%) of the landuse map.

2.2.7. Normalized difference vegetation index

NDVI is defined by

$$NDVI = (NIR - VIS) / (NIR + VIS), \quad (4)$$

where NIR is the reflectance of the Earth's surface in the near infrared channel (0.725–1.1 μm) and VIS is the reflectance in the visible portion of the spectrum or the red channel (0.5–0.68 μm) (Tucker & Sellers 1986). The NDVI map of the current study was produced from Landsat 7 ETM+ image (acquired in 1999.12.10). The NDVI was reclassified into five divisions including: < 0.1, 0.1–0.2, 0.2–0.3, 0.3–0.4, and > 0.4 (Figure 4f).

2.2.8. Lithology

It is widely recognized that the erodibility degree of rocks is the main criterion of lithology type. Landslides are heavily influenced by rock properties and its change, and most scholars had taken lithology as an important factor in landslide susceptibility mapping (Chen et al. 2011). The lithology map of Suichuan area was obtained from China Geology Organization (<http://gsd.cgs.cn>) (Figure 5 and Table 1). The lithological units of the study area were consisted of ten classes (A, B, C, D, E, F, G, H, I and J) (Table 1). About 45.8% of the lithology covering the study area falls within the unit described as class J (Eight village group high group; Eight village group Stone Group) which includes: grey, greyish green sandstones, with grey green silty slate, slate and a small amount of carbonaceous slate: grey green striped strip slate with metaclastics, bottom common lenticular limestone (Table 1).

Also, 20.3% of the study area is covered by class G (The waterwheel, Guidong, snow top super unit; The ZuoAnchao estuary, Nanping Hill unit unitunit, large clutch unit; Tang Huchao unit, Fu Fangchao unit car brain unit high delta unit; Fu Fangchao unit Gaoping unit, cat nasal Yin unit), which including monzoniticgranite; granodiorite; Tonalite diorite, porphyritic granodiorite, granite, porphyritic two porphyritic moyite; monzonitic granite. Other units constitute about 33.9% of the study area (Figure 5 and Table 1).

3. Landslide susceptibility modeling

3.1. Support vector machine

SVM is a training machine learning method. It applied for the linearly separable case analysis for linear non separable, nonlinear mapping algorithm by using low-dimensional input space. It can be

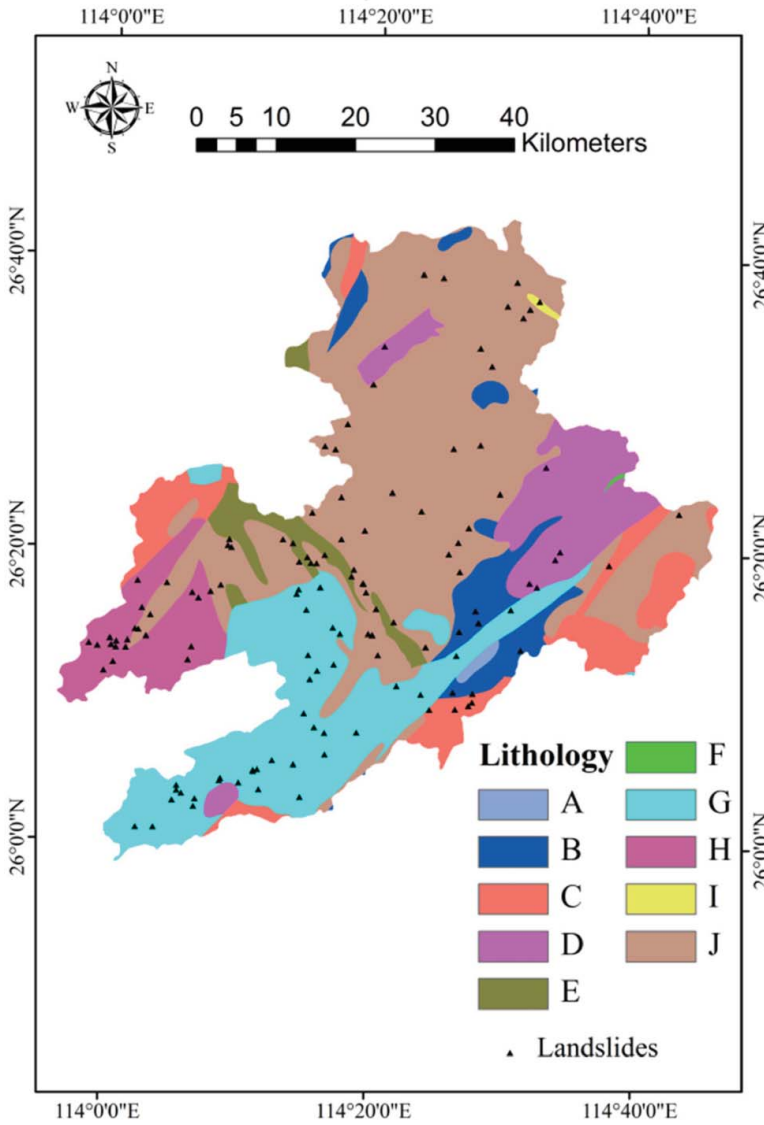


Figure 5. Lithology map of the study area.

linearly inseparable sample into high-dimensional feature space in which the linear separable, so that the high-dimensional feature space by nonlinear characteristics of the samples of the linear algorithm for linear analysis become possible (Micheletti et al. 2014). The two classes $\{1, -1\}$ denote landslide pixels and no-landslide pixels. The aim of the SVM classification is to find an optimal separating hyper plane that can distinguish the two classes, i.e. landslides and no landslides $\{1, -1\}$, from the mentioned set of training data. For the case of linear separable data, a separating hyper plane can be defined as

$$y_i(w \cdot x_i + b) / \geq 1 - \xi_i, \tag{5}$$

where w is a coefficient vector that determines the orientation of the hyper plane in the feature space, b is the offset of the hyper plane from the origin, and ξ_i is the positive slack variables (Cortes and Vapnik 1995). The determination of an optimal hyper plane leads to the solving of the following

optimization (Equations 6 and 7) problem using Lagrangian multipliers (Samui 2008):

$$\text{Minimize } \sum_{i=1}^n a_i - \frac{1}{2} \sum_{i=1}^n \sum_{j=1}^n a_i a_j y_i y_j (x_i x_j), \quad (6)$$

$$\text{Subject to } \sum_{i=1}^n a_i y_i = 0, \quad 0 \leq a_i \leq C \quad (7)$$

where α_i is Lagrange multipliers, C is the penalty, and the slack variables ξ_i allows for penalized constraint violation. The decision function, which will be used for the classification of new data, can then be written as

$$g(x) = \text{sign} \left(\sum_{i=1}^n y_i a_i x_i + b \right) \quad (8)$$

In cases when it is impossible to find the separating hyper plane using the linear kernel function, the original input data may be transferred into a high-dimension feature space through some non-linear kernel functions. The classification decision function is then written as

$$g(x) = \text{sign} \left(\sum_{i=1}^n y_i a_i K(x_i, y_i) + b \right) \quad (9)$$

where $K(x_i, x_j)$ is the kernel function

In the present study, to perform the landslide susceptibility mapping using SVM, SVM classifier provides four types of kernels including radial basis function (RBF), PL, SIG, and linear (LN). The mathematical representation of each kernel (RBF, PL, SIG, and LN) is listed as follows (Pourghasemi et al. 2013):

$$\text{Radial basis function : } K(x_i, y_i) = (-\gamma \|X_i - X_j\|), \quad \gamma > 0, \quad (10)$$

$$\text{Polynomial : } K(x_i, y_i) = (\gamma X_i^T X_j + r)^d, \quad \gamma > 0, \quad (11)$$

$$\text{Sigmoid : } K(x_i, y_i) = \tanh(\gamma X_i^T X_j + r), \quad (12)$$

$$\text{Linear : } K(x_i, y_i) = X_i^T X_j, \quad (13)$$

where $K(x_i, x_j)$ is the kernel function; γ is the gamma term in the kernel function for all kernel types except linear; d is the PL degree term in the kernel function for the PL kernel; r is the bias term in the kernel function for the PL and SIG kernels; γ , d , and r , are user-controlled parameters, as their correct definition significantly increases the accuracy of the SVM solution.

3.2. Preparation of training and validation datasets

In the present study, 178 landslide events were randomly split into two parts, out of which, 125 landslides (70%) were randomly selected for modeling construction and the remaining 53 landslides (30%) were used for the model validation. These landslides were assigned value of '1.' Since the landslide modeling using SVMs is considered as binary classification, in which the resulting models will classify pixels into two classes, 'landslide' and 'non-landslide', therefore it is necessary to collect non-landslide points (Tien Bui et al. 2016). The non-landslide areas were identified with the usage of Google Earth[®] and the analysis of high-resolution DEMs. The areas that potentially are classified as non-landslide areas are characterized by gentle and without any changes morphometric characteristic. The height difference, the steepness, and the orientation of slopes and also the absence of

concavities and convexities, are the main criteria for identifying the non-landslide areas. To avoid bias, the same number of non-landslide points was randomly generated from the landslide-free area using GIS tools and were assigned value of ‘-1’ (Tien Bui et al. 2016). Finally, values of the 15 landslide conditioning factors were extracted for all the landslide pixels and the non-landslide points to obtain the training and validation datasets.

3.3. Landslide susceptibility mapping

In this research, SVM with four types of kernel classifiers including RBF, PL, SIG, linear (LN), and PL (six select degrees were used degree 1, degree 2, degree3, degree 4, degree 5, and degree 6) were used in a GIS platform for landslide susceptibility mapping. A total of 178 landslides were mapped using field survey. Fifteen landslide conditioning factors were considered including slope-angle, altitude, slope-aspect, TWI, STI, SPI, plan curvature, profile curvature, distance to rivers, distance to faults, distance to roads, precipitation, landuse, NDVI, and lithology.

The results of spatial relationship between landslide occurrences and conditioning factors using frequency ratio model is shown in Table 2. In Table 2, for the slope-angle class 0–5°, the frequency ratio was 0.70 which indicates a very low probability of landslide occurrence. Similarly, for the slope-angle class 5°–15°, the ratio was 1.31; where the probability of landslide occurrence is high. The frequency ratio between landslide occurrence and altitude showed that the altitude class between 200 and 400 m had the highest FR value 1.11 and for altitude class 600–800 m the FR had the lowest value (0.69). The frequency ratio for the slope-aspect was high for southeast-facing and south-facing slopes (FR value of 1.39 and 1.27, respectively) but the FR was low for flat class (0.00). The frequency ratio for the TWI, SPI, and STI were high for classes 7–11, 40–60, and 10–30, respectively, where the FR values were 1.07, 1.28, and 1.06, respectively.

Table 2. Frequency ratio values of landslide-conditioning factors.

Factor	Class	No. of pixels in domain	No. of landslides	% Pixels	% LS	FR
Slope-angle (degree)	0–5°	456763	8	0.0918	0.06	0.70
	5–15°	1031810	34	0.2073	0.27	1.31
	15–30°	2589367	66	0.5203	0.53	1.01
	>30°	898377	17	0.1805	0.14	0.75
Altitude (m)	<200	851521	22	0.1711	0.18	1.03
	200–400	1978056	55	0.3975	0.44	1.11
	400–600	1033201	22	0.2076	0.18	0.85
	600–800	461607	8	0.0928	0.06	0.69
	>800	651932	18	0.1310	0.14	1.10
Slope aspect	Flat	1957	0	0.0004	0.00	0.00
	North	646837	12	0.1300	0.10	0.74
	Northeast	636463	17	0.1279	0.14	1.06
	East	678147	20	0.1363	0.16	1.17
	Southeast	658780	23	0.1324	0.18	1.39
	South	595249	19	0.1196	0.15	1.27
	Southwest	558067	10	0.1121	0.08	0.71
	West	572606	10	0.1151	0.08	0.70
TWI	Northwest	628211	14	0.1262	0.11	0.89
	<7	4074951	101	0.8189	0.81	0.99
	7–11	672096	18	0.1351	0.14	1.07
SPI	>11	229270	6	0.0461	0.05	1.04
	<20	2125199	51	0.4271	0.41	0.96
	20–40	1066521	25	0.2143	0.20	0.93
	40–60	527667	17	0.1060	0.14	1.28
	60–80	276076	7	0.0555	0.06	1.01
	>80	980854	25	0.1971	0.20	1.01

(continued)

Table 2. (Continued)

Factor	Class	No. of pixels in domain	No. of landslides	% Pixels	% LS	FR
LS (m)	<10	2908914	70	0.5846	0.56	0.96
	10–30	1985884	53	0.3991	0.42	1.06
	>30	81519	2	0.0164	0.02	0.98
Plan Curvature (100\m)	Concave	2233462	54	0.4488	0.43	0.96
	Flat	62321	1	0.0125	0.01	0.64
	Convex	2680534	70	0.5387	0.56	1.04
Profile curvature (100\m)	< (-0.001)	2321846	50	0.4666	0.40	0.86
	(-0.001)–(0.001)	51737	2	0.0104	0.02	1.54
	> (0.001)	2602734	73	0.5230	0.58	1.12
Distance to rivers (m)	<100	915599	41	0.1840	0.33	1.78
	100–300	1469173	59	0.2952	0.47	1.60
	300–500	1188278	17	0.2388	0.14	0.57
	500–700	798706	4	0.1605	0.03	0.20
	>700	604561	4	0.1215	0.03	0.26
Distance to faults (m)	<500	362766	9	0.0729	0.07	0.99
	500–1000	339173	6	0.0682	0.05	0.70
	1000–2000	605905	20	0.1218	0.16	1.31
	2000–3000	508483	15	0.1022	0.12	1.17
	>3000	3159990	75	0.6350	0.60	0.94
Distance to roads (m)	<500	1595059	66	0.3205	0.53	1.65
	500–1000	1223301	22	0.2458	0.18	0.72
	1000–2000	1507225	26	0.3029	0.21	0.69
	2000–3000	490943	9	0.0987	0.07	0.73
	>3000	159789	2	0.0321	0.02	0.50
Precipitation (mm)	697.1–994.4	1372445	26	0.2758	0.21	0.75
	994.4–1140.7	1906946	35	0.3832	0.28	0.73
	1140.7–1306.5	1283941	49	0.2580	0.39	1.52
	1306.5–1545.3	337143	10	0.0677	0.08	1.18
	1545.3–1940.2	75842	5	0.0152	0.04	2.62
Land use	Farmland	314343	10	0.0632	0.08	1.27
	Bare	82036	2	0.0165	0.02	0.97
	Forest	2933531	84	0.5895	0.67	1.14
	Grass	1254800	22	0.2522	0.18	0.70
	Residential area	390513	7	0.0785	0.06	0.71
	Water	1094	0	0.0002	0.00	0.00
NDVI	<(-0.001)	1034833	20	0.2080	0.16	0.77
	(-0.001)–(0.00)	115551	4	0.0232	0.03	1.38
	(0.00)–(0.05)	464554	12	0.0934	0.10	1.03
	(0.05)–(0.10)	645954	24	0.1298	0.19	1.48
	> (0.1)	2715425	65	0.5457	0.52	0.95
Lithology	A	14792	0	0.0030	0.00	0.00
	B	265356	6	0.0533	0.05	0.90
	C	425894	5	0.0856	0.04	0.47
	D	478319	6	0.0961	0.05	0.50
	E	157814	5	0.0317	0.04	1.26
	F	2072	0	0.0004	0.00	0.00
	G	1011094	37	0.2032	0.30	1.46
	H	334072	18	0.0671	0.14	2.15
	I	6762	1	0.0014	0.01	5.89
	J	2280142	47	0.4582	0.38	0.82

In the case of plan curvature, convex has high FR value of 1.04 than concave and flat. In the case of profile curvature, most of the landslides occurred in class (-0.001) to (0.001) with FR value of 1.54. In addition, it was found that landslides at a distance to river class <100 m had a FR value of 1.78; distance to fault class of 1000–2000 m had a higher FR value of 1.31; whereas a distance to road class of <500 had the higher FR value of 1.65. In the case of precipitation, 1545.3–1940.2 class had the highest FR value of 2.62. In the case of landuse, the FR value was high in farmland area

(1.27); however, water had a lower FR value of (0.00). In the case of NDVI, the class (0.05)–(0.10) had a high FR (1.48). There were ten groups of lithological units within the study area, the FR between landslide occurrence and lithology suggests that the group I (i.e. Z (LechangXia Group)) which include Grey purple feldspar quartz sandstone intercalated with siltstone slate; light grey chert sandwiched phyllite: grey, greyish green sandstones had the highest value (5.89), whereas the group A with grey sandstone, siltstone, shale, carbonaceous shale and coal seam clamp: grey quartz conglomerate, pebbly sandstone, sandstone; purple red sandstone had the lowest value (0.00).

Finally, the landslide susceptibility maps were produced according to SVM kernels models using RBF, PL, SIG, and linear (LN). The landslide susceptibility value (LSPV) ranges from 0 to 1, the value with higher susceptibility means the higher of the landslide occurrence. Figure 6 shows 6 different degree of PL of landslide susceptibility maps, degree 1 to degree 6 were from (a) to (f), the LSPV of 6 degree were 0.0860–0.8652, 0.0905–0.8174, 0.0420–0.8674, 0.1127–0.8390, 0.1613–0.8244, and 0.1699–0.8009, respectively. Figure 7 shows the landslide susceptibility using the kernel of RBF, SIG, and linear (LN), the value of them were 0.0698–0.8864, 0.0768–0.7834, and 0.0843–0.8660, respectively.

4. Validation and comparison

In this study, the receiver-operating characteristic curve (ROC) and area under the curve (AUC) were used to evaluate and compare the performance and prediction capability of the landslide models (Pham et al. 2016, Tien Bui et al. 2016). The ROC curve is a graph that is constructed based on sensitivity and 1–specificity with different cut off values. The AUC varies from 0.5 to 1.0, the model with higher AUC is considered to be the best. Most studies in the process of validation, both the success rate and the prediction rate are used to validate and rank the models, so in current study, we use

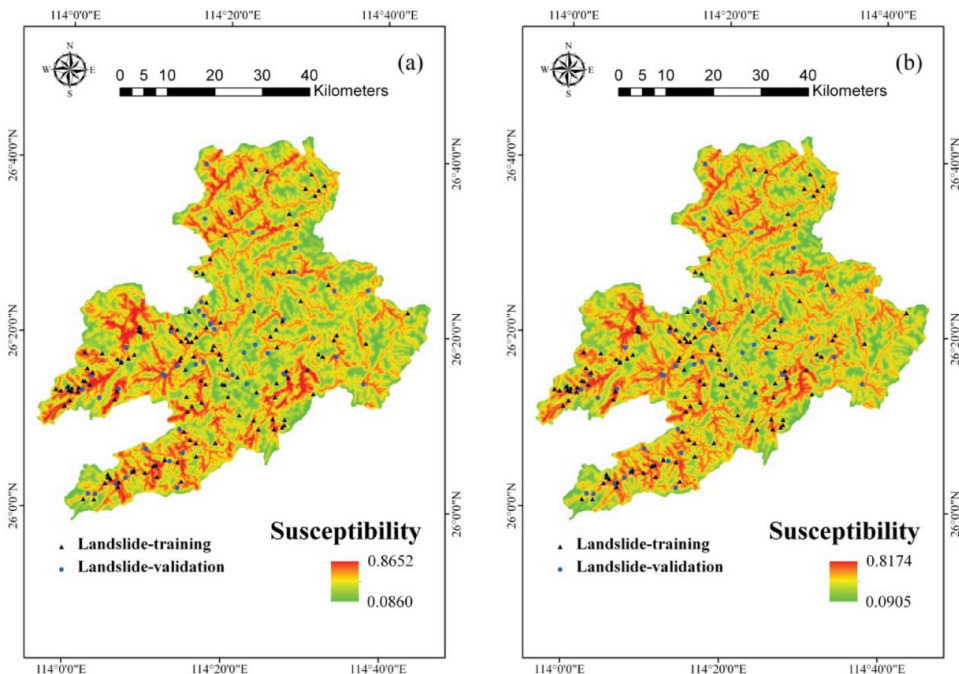


Figure 6. Landslide susceptibility maps produced by polynomial (PL) model (a) degree 1, (b) degree 2, (c) degree 3, (d) degree 4, (e) degree 5, and (f) degree 6.

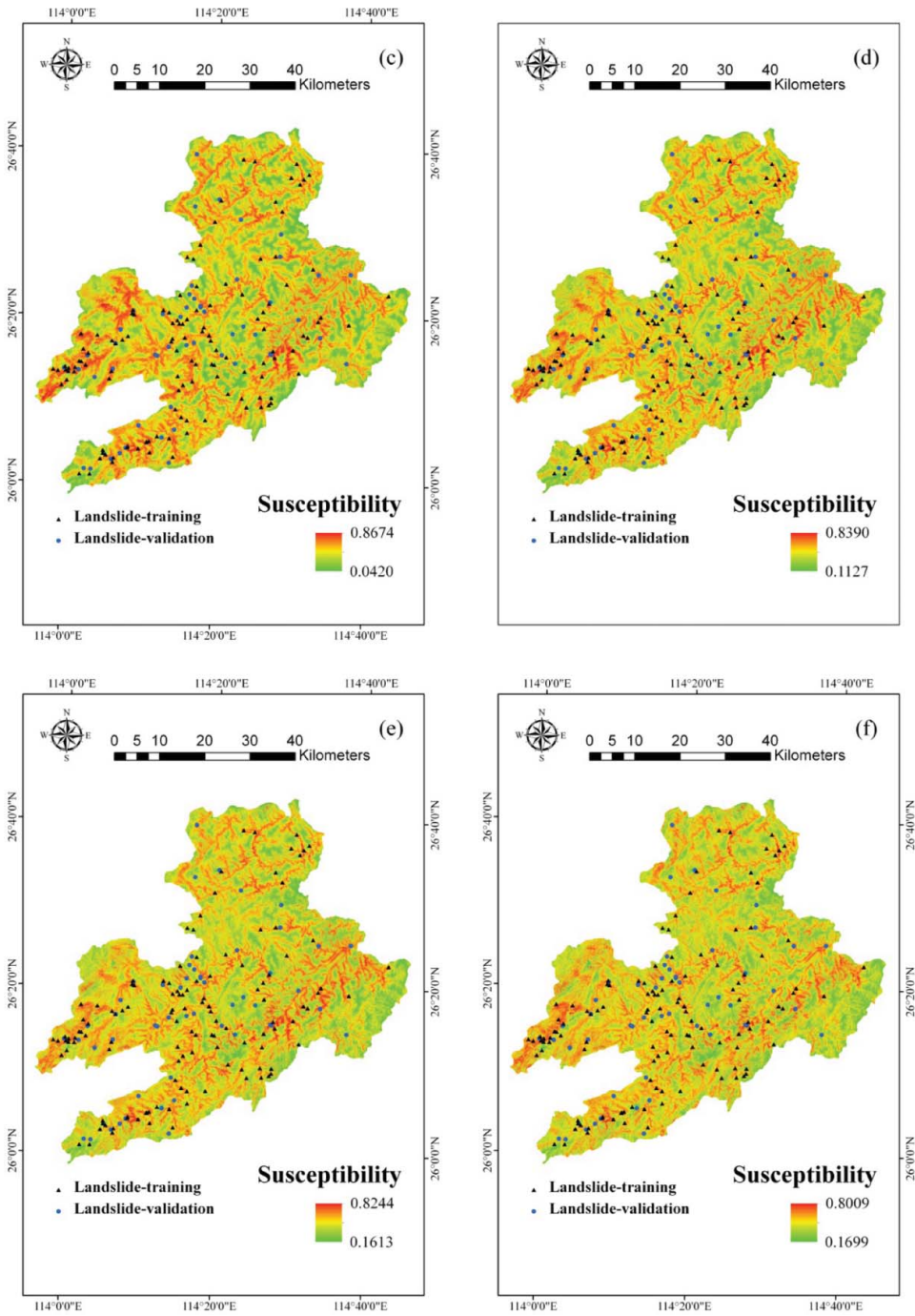


Figure 6. (Continued).

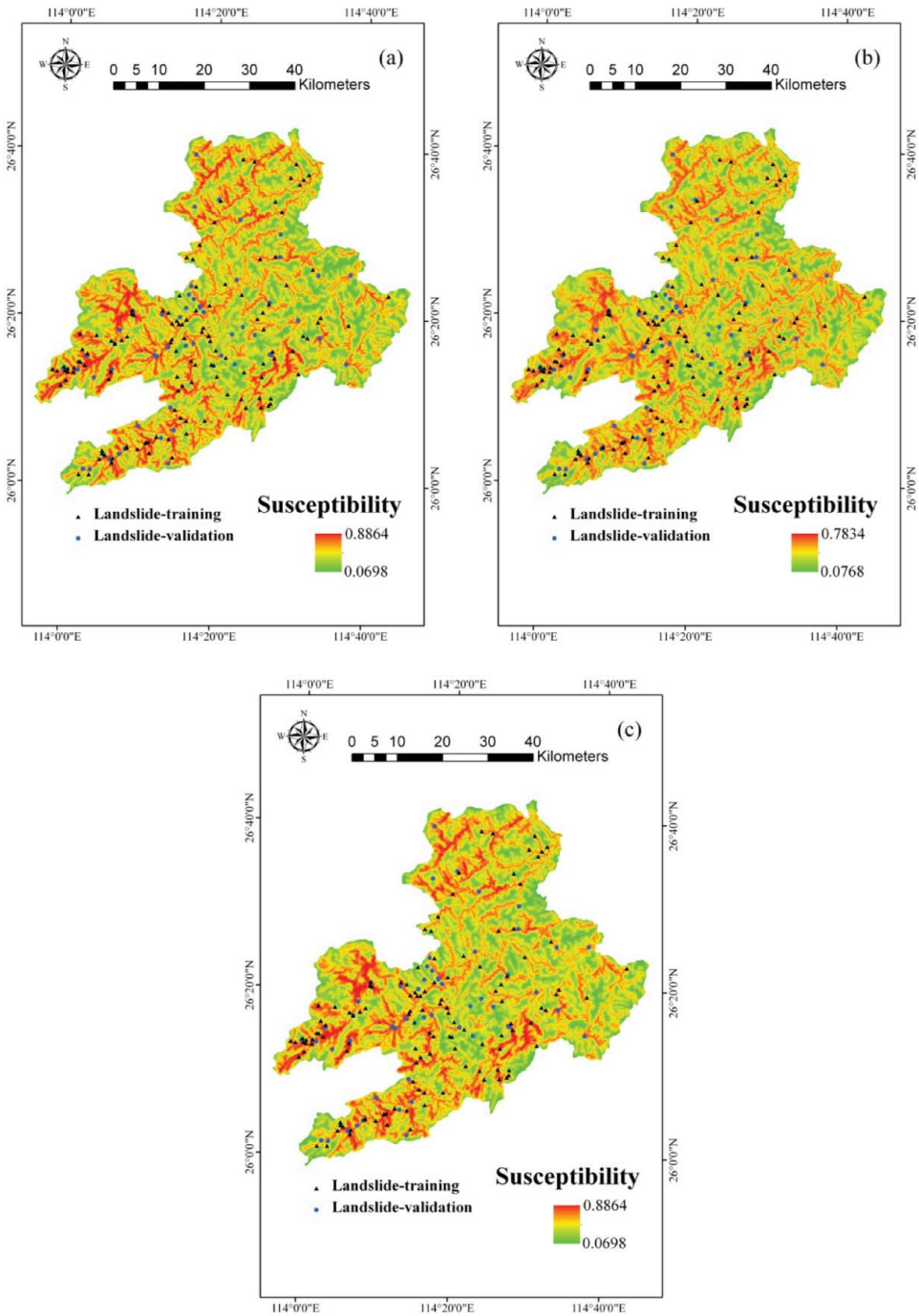


Figure 7. Landslide susceptibility maps produced by other models including (a) sigmoid function (SIG), (b) radial basis function (RBF), and (c) linear function (LN).

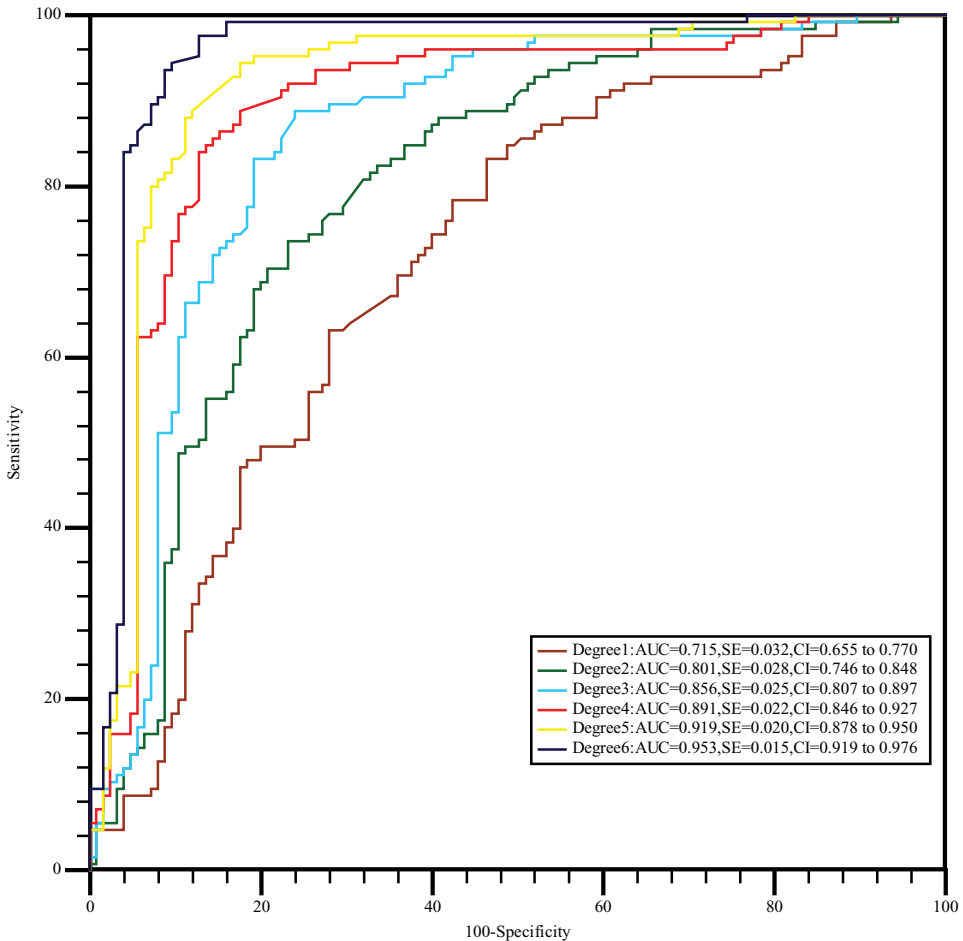


Figure 8. Success rate curves for the landslide potential maps by polynomial function (PL): degree1, degree 2, degree 3, degree 4, degree 5, and degree 6.

both of them. It is noted that the success rate and the prediction rate here are derived from the ROC curve that are different with those mentioned in Chung and Fabbri (2003).

The success rate results were obtained by estimating AUC of these susceptibility models using the training dataset, whereas the prediction rate results were derived in the same way but using the validation dataset. Figure (8) shows the success rate curves for the six different degree of PL kernel, degree 6 has the highest AUC (0.953), degree 1 has the lowest AUC (0.715). Figure (9) shows the other kernel named SIG, RBF, and Linear, the value of AUC were 0.680, 0.833, 0.716, respectively. The prediction rate showed in Figures 10 and 11, the value of 6 degree of PL was 0.738, 0.730, 0.683, 0.648, 0.608, and 0.598, respectively; the value of SIG, RBF, and Linear were 0.741, 0.716 and 0.740, respectively.

5. Discussions and conclusions

Landslides susceptibility map is considered as a valuable tool for land use planning and management (Akgun 2012), therefore these maps should be produced by high performance models. However, it is still difficult to obtain landslide models with high accuracy because landslide is non-linear and complex process that relates to various conditioning factors (Tien Bui et al. 2016). Literature review

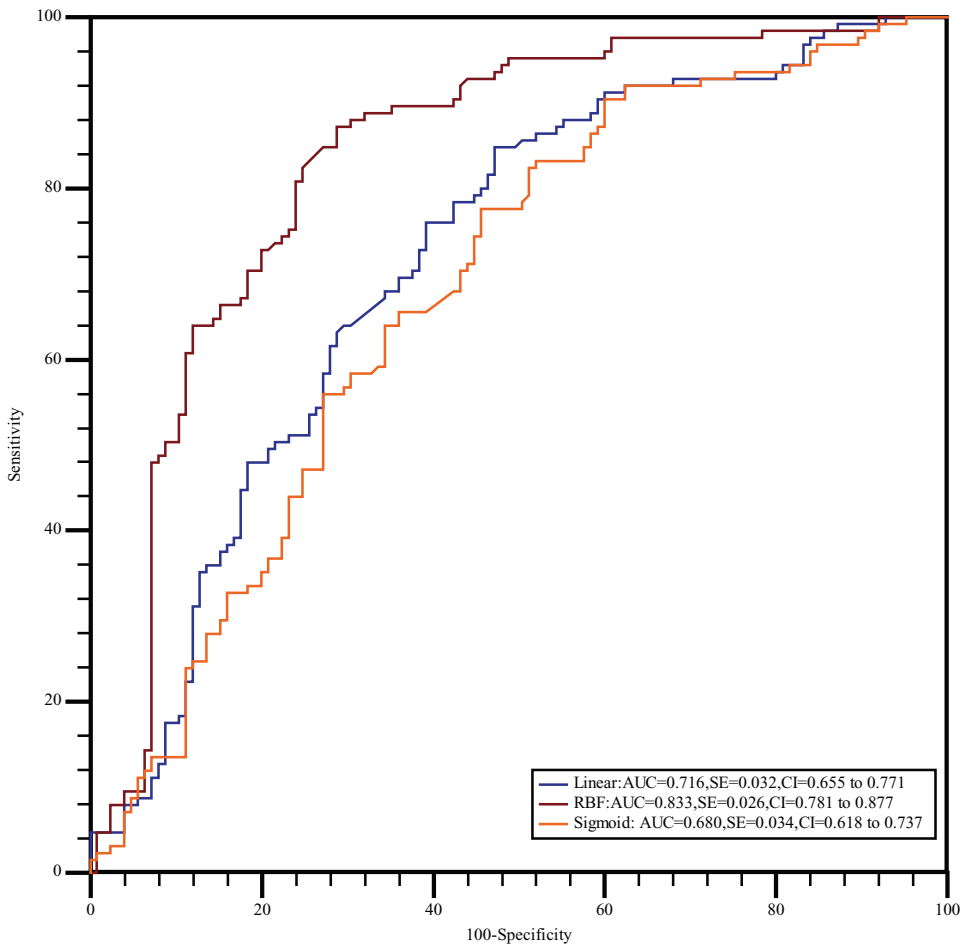


Figure 9. Success rate curves for the landslide potential maps by linear function (LN), radial basis function (RBF), and sigmoid function (SIG).

shows that although no method or technique is the best for all regions; however, SVMs are considered to be the most efficient methods and have proven outperforming conventional methods for susceptibility mapping (Hoang & Tien Bui 2016; Tien Bui et al. 2012; Yao et al. 2008). It is well-known that performance of SVM models is strongly influenced by the kernel function used and its parameters. However, investigation of kernel functions in SVM models for landslide susceptibility modeling is still rare. We fill this gap in literature by investigating and comparing four kernel functions (RBF, PL, SG, and LN) used in SVMs with a case study at the Suichuan area, the Jiangxi province (China).

To obtain this purpose, a landslide database with 178 landslide location and 15 conditioning factors has been established, and then, used to build and validate different SVM models. The results show that performance of landslide models is strongly depended on kernel function used. For the case of the PL function, a total of 6 degrees have been checked and the model with the first degree of the PL function has lowest degree of fit, but has the highest prediction capability. The finding in this study shows that the higher the degree of the PL function, the better performance of the model on the training data is (Figure 7). In contrast to results in the training dataset, the prediction capability of the model in the validation dataset decreases when the degree of the PL function increases. This indicates that the models with high degree of the PL function are suffered from overfitting problem.

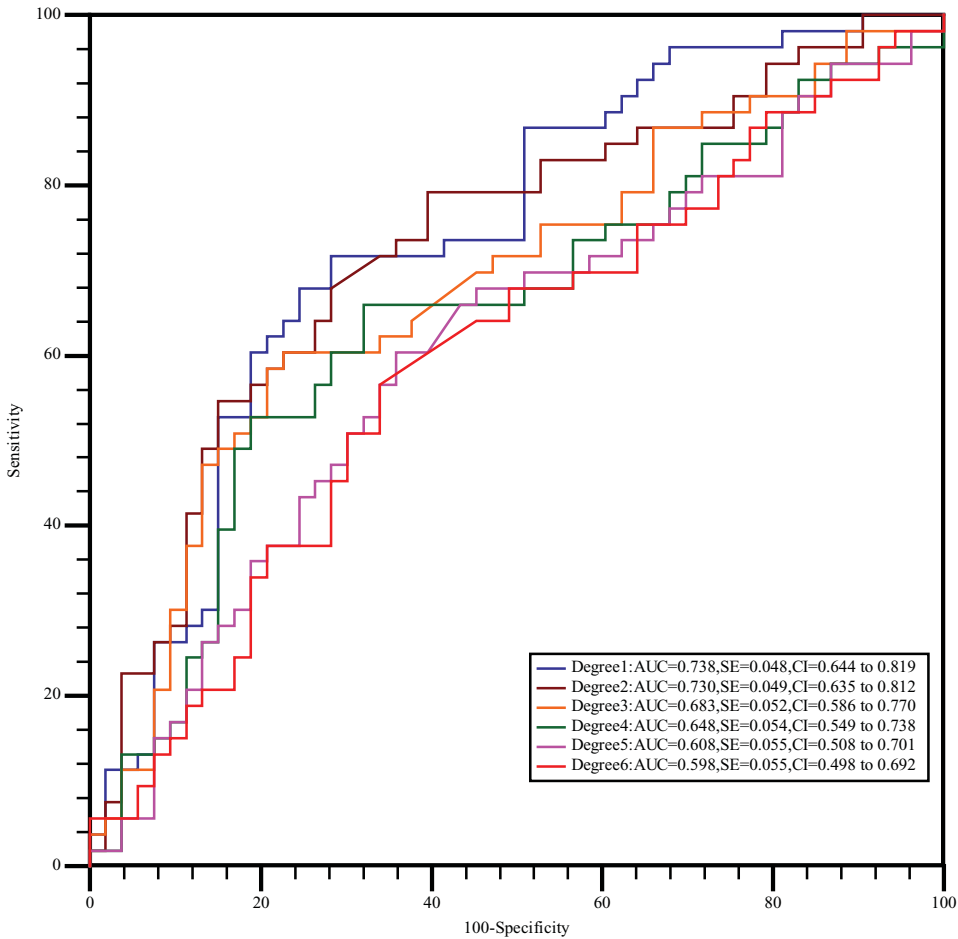


Figure 10. Prediction rate curves for the landslide potential maps by polynomial function (PL): degree1, degree 2, degree 3, degree 4, degree 5, and degree 6.

It is noted that SVM models aim to build hyperplanes that separates pixels into two classes, 'landslide' and 'non-landslide.' With higher degree of the PL function, more training samples (called support vectors) lies on the hyperplanes and therefore increasing loss of generality. Consequently, the prediction capability of the models is decreased.

For the case of the SVM models with LN, RBF, and SIG function, although the model with RBF has the highest performance with $AUC = 0.833$ (followed by SVM-LN with $AUC = 0.716$ and SVM-SIG with $AUC = 0.680$); however, prediction capability checking show that the SVM-RBF model is slightly ($\sim 2\%$) lower than the SVM-LN model and the SVM-SIG model. Problem of over-fitting of these models is alleviated since the difference of these AUCs in the training and validation datasets are low. Based on the above analysis, we conclude that the SVM-RBF model is the best for this study. This finding is in agreement with some landslide studies such as Tien Bui et al. (2012) and Hong et al. (2016) who stated that the SVM models with RBF function has the highest prediction capability.

In fact, performance of the SVM-RBF model is influenced by the selection of C and γ parameter values (see Section 3.1) and in this study, these parameters were derived using the grid-search technique. Therefore, the performance of the SVM-RBF model could be enhanced if the process of picking up C and γ is carried out using new optimization techniques (Hoang et al. 2016). Thus, future

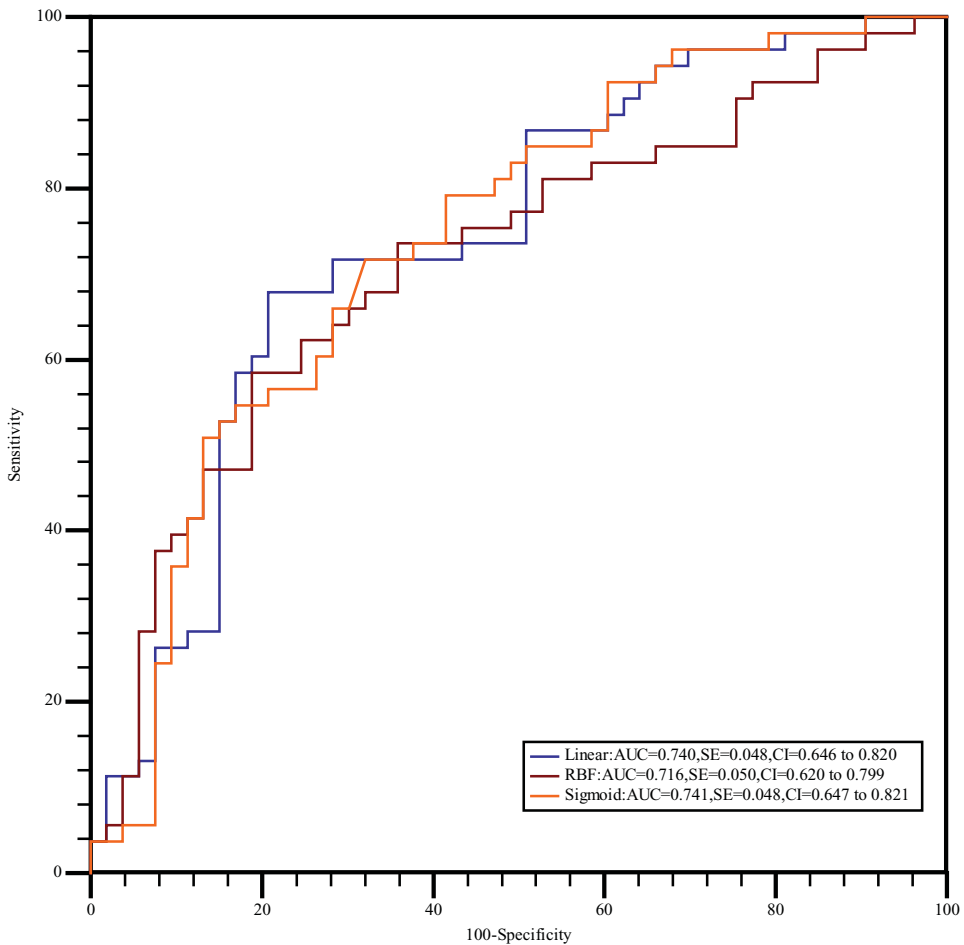


Figure 11. Prediction rate curves for the landslide potential maps by linear function (LN), radial basis function (RBF), and sigmoid function (SIG).

studies on application of SVMs for landslide susceptibility mapping should focus on using soft computing optimization techniques to optimize kernel parameters values.

Overall, this study contributes to the body knowledge of landslide susceptibility by investigating potential application of SVMs with four kernel functions with a case study at southwest China. According to this study, the SVM model with RBF function is the best suit for the data at hand, followed by the SVM model with second degree PL, the SVM model with LN, and the SVM model with SIG. At final conclusion, the result from this study is useful for land use planning and management in landslide-prone areas.

Acknowledgments

The authors would like to express their gratitude to the Editor in Chief and the anonymous reviewers for their helpful comments on the manuscript.






Disclosure statement

No potential conflict of interest was reported by the authors.

Funding

This research was supported by the National Natural Science Foundation of China [grant number 41472202], [grant number 41202235]; the Doctoral Scientific Research Foundation of Xian University of Science and Technology [grant number 2015QDJ067]; and General Program of Jiangxi Meteorological Bureau.

ORCID

Haoyuan Hong  <http://orcid.org/0000-0001-6224-069X>
 Biswajeet Pradhan  <http://orcid.org/0000-0001-9863-2054>
 Dieu Tien Bui  <http://orcid.org/0000-0001-5161-6479>
 Chong Xu  <http://orcid.org/0000-0002-3956-4925>
 Wei Chen  <http://orcid.org/0000-0002-5825-1422>

Reference

- Akgun A. 2012. A comparison of landslide susceptibility maps produced by logistic regression, multi-criteria decision, and likelihood ratio methods: a case study at Izmir, Turkey. *Landslides*. 9:93–106.
- Alkhasawneh MS, Ngah UK, Tay LT, Mat Isa NA, Al-Batah MS. 2014. Modeling and testing landslide hazard using decision tree. *J Appl Math*. 2014:568–575.
- Althuwaynee OF, Pradhan B, Lee S. 2012. Application of an evidential belief function model in landslide susceptibility mapping. *Comput Geosci*. 44:120–135.
- Carey JM, Petley DN. 2014. Progressive shear-surface development in cohesive materials: implications for landslide behaviour. *Eng Geol*. 177:54–65.
- Chena H, Lina GW, Lua MH, Shiha TY, Horngb MJ, Wuc SJ. 2011. Effects of topography, lithology, rainfall and earthquake on landslide and sediment discharge in mountain catchments of Southeastern Taiwan. *Geomorphology*. 133:132–142.
- Chen W, Chai H, Zhao Z, Wang Q, Hong H. 2016a. Landslide susceptibility mapping based on GIS and support vector machine models for the Qianyang County, China. *Environ Earth Sci*. 75:1–13.
- Chen W, Ding X, Zhao R, Shi S. 2016b. Application of frequency ratio and weights of evidence models in landslide susceptibility mapping for the Shangzhou District of Shangluo City, China. *Environ Earth Sci*. 75:1–10.
- Chen W, Li W, Chai H, Hou E, Li X, Ding X. 2016c. GIS-based landslide susceptibility mapping using analytical hierarchy process (AHP) and certainty factor (CF) models for the Baozhong region of Baoji City, China. *Environ Earth Sci*. 75:1–14.
- Chung C-JF, Fabbri AG. 2003. Validation of spatial prediction models for landslide hazard mapping. *Natural Hazards*. 30:451–472.
- Coe JA. 2012. Regional moisture balance control of landslide motion: implications for landslide forecasting in a changing climate. *Geology*. 40:323–326.
- Cortes C, Vapnik V. 1995. Support vector network. *Mach Learn*. 20:273–297.
- Conoscenti C, Angileri S, Cappadonia C, Rotigliano E, Agnesi V, Märker M. 2014. Gully erosion susceptibility assessment by means of GIS-based logistic regression: a case of Sicily (Italy). *Geomorphology*. 204:399–411.
- Constantin M, Bednarik M, Jurchescu MC, Vlaicu M. 2011. Landslide susceptibility assessment using the bivariate statistical analysis and the index of entropy in the Sibiciu Basin (Romania). *Environ Earth Sci*. 63:397–406.
- Demir G, Aytakin M, Akgün A, İkizler SB, Tatar O. 2013. A comparison of landslide susceptibility mapping of the eastern part of the North Anatolian fault zone (Turkey) by likelihood-frequency ratio and analytic hierarchy process methods. *Nat Hazards*. 154:417–441.
- Ding H, Li Y, Ni S, Ma G, Shi Z, Zhao G, Yan L, Yan Z. 2014. Increased sediment discharge driven by heavy rainfall after Wenchuan earthquake: a case study in the upper reaches of the min river, Sichuan, China. *Quat Int*. 333:122–129.
- Dong G, Zhang F, Ma M, Fan Y, Zhang J, Wang Z, Chen F. 2014. Ancient landslide-dam events in the Jishi gorge, upper yellow river valley, China. *Quat Res*. 81:445–451.
- Ercanoglu M, Temiz FA. 2011. Application of logistic regression and fuzzy operators to landslide susceptibility assessment in Azdavay (Kastamonu, Turkey). *Environ Earth Sci*. 64:949–964.
- Feuillet T, Coquin J, Mercier D, Cossart E, Decaulne A, Jonsson HP, Saemundsson, B. 2014. Focusing on the spatial non-stationarity of landslide predisposing factors in Northern Iceland: Do paraglacial factors vary over space? *Prog Phys Geog*. 38:354–377.
- Hadmoko DS, Lavigne F, Sartohadi J, Hadi P, Winaryo. 2010. Landslide hazard and risk assessment and their application in risk management and landuse planning in eastern flank of Menoreh mountains, Yogyakarta province, Indonesia. *Nat Hazards*. 54:623–642.

- Hapke CJ, Green KR. 2006. Coastal landslide material loss rates associated with severe climatic events. *Geology*. 34:1077–1080.
- Hassaballa AA, Althuwaynee OF, Pradhan B. 2014. Extraction of soil moisture from RADARSAT-1 and its role in the formation of the 6 December 2008 landslide at Bukit Antarabangsa, Kuala Lumpur. *Arabian J Geosci*. 7:2831–2840.
- Hoang ND, Tien Bui D, Liao KW. 2016. Groutability estimation of grouting processes with cement grouts using differential flower pollination optimized support vector machine. *Appl Soft Comput*. 45:173–186.
- Hong H, Pradhan B, Jebur MN, Tien Bui D, Xu C, Akgun A. 2016. Spatial prediction of landslide hazard at the Luxi area (China) using support vector machines. *Environ Earth Sci*. 75:1–14.
- Hong H, Pradhan B, Xu C, Tien Bui D. 2015. Spatial prediction of landslide hazard at the Yihuang area (China) using two-class kernel logistic regression, alternating decision tree and support vector machines. *Catena*. 133:266–281.
- Huang B, Yin Y, Chen X, Liu G, Wang S, Jiang Z. 2014. Experimental modeling of tsunamis generated by subaerial landslides: two case studies of the three gorges reservoir, china. *Environ Earth Sci*. 71:3813–3825.
- Kavzoglu T, Sahin EK, Colkesen I. 2014. Landslide susceptibility mapping using GIS-based multi-criteria decision analysis, support vector machines, and logistic regression. *Landslides*. 11:425–439.
- Klose M, Gruber D, Damm B, Gerold G. 2014. Spatial databases and GIS as tools for regional landslide susceptibility modeling. *Zeitschrift Für Geomorphologie*. 58:1–36.
- Paulín GL, Bursik M, Hubp JL, Mejía LMP, Quesada FA. 2014. A GIS method for landslide inventory and susceptibility mapping in the río el estado watershed, pico de orizaba volcano, México. *Nat Hazards*. 71:229–241.
- Li C, Tang H, Ge Y, Hu X, Wang L. 2014. Application of back-propagation neural network on bank destruction forecasting for accumulative landslides in the three gorges reservoir region, china. *Stochastic Environ Res Risk Assess*. 28:1465–1477.
- Li XZ, Kong JM. 2014. Application of GA-SVM method with parameter optimization for landslide development prediction. *Nat Hazards Earth Syst Sci*. 14:525–533.
- Lissak C, Maquaire O, Malet JP, Bitri A, Samyn K, Grandjean G, Bourdeau C, Reiffsteck P, Davidson R. 2014. Airborne and ground-based data sources for characterizing the morpho-structure of a coastal landslide. *Geomorphology*. 217:140–151.
- May C, Roering J, Eaton LS, Burnett KM. 2013. Controls on valley width in mountainous landscapes: the role of landsliding and implications for salmonid habitat. *Geology*. 41:503–506.
- Miao H, Wang G, Yin K, Kamai T, Li Y. 2014. Mechanism of the slow-moving landslides in Jurassic red-strata in the three gorges reservoir, China. *Eng Geol*. 171:59–69.
- Michel GP, Kobiyama M, Goerl RF. 2014. Comparative analysis of SHALSTAB and SINMAP for landslide susceptibility mapping in the Cunha River basin, southern Brazil. *J Soils Sediments*. 14:1266–1277.
- Micheletti N, Foresti L, Robert S, Leuenberger M, Pedrazzini A, Jaboyedoff M, Kanevski M. 2014. Machine learning feature selection methods for landslide susceptibility mapping. *Math Geosci*. 46:33–57.
- Moore ID, Grayson RB. 1991. Terrain-based catchment partitioning and runoff prediction using vector elevation data. *Water Resour Res*. 27:1177–1191.
- Moretti L, Mangeney A, Capdeville Y, Stutzmann E, Huggel C, Schneider D, Bouchut F. 2012. Numerical modeling of the mount steller landslide flow history and of the generated long period seismic waves. *Geophys Res Lett*. 39:276–289.
- Muceku Y, Korini O. 2014. Landslide and slope stability evaluation in the historical town of Kruja, Albania. *Nat Hazards Earth SystSci*. 14:545–556.
- Neuhaeuser B, Damm B, Terhorst B. 2012. GIS-based assessment of landslide susceptibility on the base of the weights-of-evidence model. *Landslides*. 9:511–528.
- Pedrazzini A, Jaboyedoff M, Loye A, Derron MH. 2013. From deep seated slope deformation to rock avalanche: destabilization and transportation models of the Sierre landslide (Switzerland). *Tectonophysics*. 605:149–168.
- Peng L, Niu R, Huang B, Wu X, Zhao Y, Ye R. 2014. Landslide susceptibility mapping based on rough set theory and support vector machines: a case of the three gorges area, China. *Geomorphology*. 204:287–301.
- Perrone A, Lapenna V, Piscitelli S. 2014. Electrical resistivity tomography technique for landslide investigation: a review. *Earth-Sci Rev*. 135:65–82.
- Pham BT, Tien Bui D, Pourghasemi HR, Indra P, Dholakia MB. 2015. Landslide susceptibility assessment in the Uttarakhand area (India) using GIS: a comparison study of prediction capability of naïve Bayes, multilayer perceptron neural networks, and functional trees methods. *Theor Appl Climatol*. DOI: 10.1007/s00704-015-1702-9.
- Pham BT, Pradhan B, Tien Bui D, Prakash I, Dholakia MB. 2016. A comparative study of different machine learning methods for landslide susceptibility assessment: a case study of Uttarakhand area (India). *Environ ModellSoftw*. 84:240–250.
- Poudyal CP, Chang C, Oh HJ, Lee S. 2010. Landslide susceptibility maps comparing frequency ratio and artificial neural networks: a case study from the Nepal Himalaya. *Environ Earth Sci*. 61:1049–1064.
- Pourghasemi HR, Jirandeh AG, Pradhan B, Xu C, Gokceoglu C. 2013. Landslide susceptibility mapping using support vector machine and GIS at the Golestan province, Iran. *J Earth Syst Sci*. 122:349–369.

- Pourghasemi HR, Mohammady M, Pradhan B. 2012a. Landslide susceptibility mapping using index of entropy and conditional probability models in GIS: Safarood Basin, Iran. *Catena*. 97:71–84
- Pourghasemi HR, Pradhan B, Gokceoglu C. 2012b. Application of fuzzy logic and analytical hierarchy process (AHP) to landslide susceptibility mapping at Haraz watershed, Iran. *Nat Hazards*. 63:965–996.
- Pradhan B. 2011. Manifestation of an advanced fuzzy logic model coupled with geoinformation techniques for landslide susceptibility analysis. *Environ Ecol Stat*. 18:471–493.
- Pradhan B, Lee S. 2010. Landslide susceptibility assessment and factor effect: back-propagation artificial neural networks and their comparison with frequency ratio and bivariate logistic regression modeling. *Environ Modell Softw*. 25:747–759.
- Pradhan B, Abokharima MH, Jebur MN, Tehrany MS. 2014. Land subsidence susceptibility mapping at Kinta valley (Malaysia) using the evidential belief function model in GIS. *Nat Hazards*. 73:1019–1042.
- Raia S, Alvioli M, Rossi M, Baum RL, Godt JW, Guzzetti F. 2013. Improving predictive power of physically based rainfall-induced shallow landslide models: a probabilistic approach. *Geosci Model Dev Dis*. 7:495–514.
- Samui P. 2008. Slope stability analysis: a support vector machine approach. *Environ Geol*. 56:255–267
- Scheingross JS, Minchew BM, Mackey BH, Simons M, Lamb MP, Hensley S. 2013. Fault-zone controls on the spatial distribution of slow-moving landslides. *Geol SocAm Bull*. 125:473–489.
- Shahabi H, Khezri S, Ahmad BB, Hashim M. 2014. Landslide susceptibility mapping at central Zab Basin, Iran: a comparison between analytical hierarchy process, frequency ratio and logistic regression models. *Catena*. 115:55–70.
- Tehrany MS, Pradhan B, Jebur MN. 2014. Flood susceptibility mapping using a novel ensemble weights-of-evidence and support vector machine models in GIS. *J Hydrol*. 512:332–343.
- Tien Bui D, Anh Tuan T, Hoang ND, Quoc Thanh N, Nguyen BD, Van Liem N, Pradhan B. 2016. Spatial prediction of rainfall-induced landslides for the Lao Cai area (Vietnam) using a novel hybrid intelligent approach of least squares support vector machines inference model and artificial bee colony optimization. *Landslides*. 1–12. Doi: 10.1007/s10346-016-0711-9.
- Tien Bui D, Pradhan B, Lofman O, Revhaug I. 2012. Landslide susceptibility assessment in Vietnam using support vector machines, decision tree, and naïve Bayes models. *Math Probl Eng*. 2012:1–27.
- Tien Bui D, Tuan TA, Klempe H, Pradhan B, Revhaug I. 2016. Spatial prediction models for shallow landslide hazards: a comparative assessment of the efficacy of support vector machines, artificial neural networks, kernel logistic regression, and logistic model tree. *Landslides*. 13:361–378.
- Tien Bui D, Pham TB, Nguyen QP, Hoang ND. 2016. Spatial prediction of rainfall-induced shallow landslides using hybrid integration approach of least squares support vector Machines and differential evolution optimization: a case study in central Vietnam. *Int J Dig Earth*. 1–22. Doi: 10.1080/1753894720161169561.
- Tucker C, Sellers P. 1986. Satellite remote sensing of primary production. *Int J Remote Sens*. 7:1395–1416.
- Umar Z, Pradhan B, Ahmad A, Jebur MN, Tehrany MS. 2014. Earthquake induced landslide susceptibility mapping using an integrated ensemble frequency ratio and logistic regression models in west Sumatera Province, Indonesia. *Catena*. 118:124–135.
- Weng MC, Wu MH, Ning SK, Jou YW. 2011. Evaluating triggering and causative factors of landslides in Lawnon River Basin, Taiwan. *Eng Geol*. 123:72–82.
- West AJ, Hetzel R, Li G, Jin Z, Zhang F, Hilton RG, Densmore AL. 2014. Dilution of 10 be in detrital quartz by earthquake-induced landslides: implications for determining denudation rates and potential to provide insights into landslide sediment dynamics. *Earth Planet Sci Lett*. 396:143–153.
- Xu C, Dai F, Xu X, Yuan HL. 2012. GIS-based support vector machine modeling of earthquake-triggered landslide susceptibility in the Jianjiang river watershed, china. *Geomorphology*. 145–146:70–80.
- Xu C, Xu X. 2014a. The spatial distribution pattern of landslides triggered by the 20 April 2013 Lushan earthquake of China and its implication to identification of the seismogenic fault. *Chin Sci Bull*. 59:1416–1424.
- Xu C, Xu X. 2014b. Statistical analysis of landslides caused by the Mw 6.9 Yushu, China, earthquake of April 14, 2010. *Nat Hazards*. 72:871–893.
- Xu C, Xu X, Pourghasemi HR, Pradhan B, Iqbal J. 2013a. Volume, gravitational potential energy reduction, and regional centroid position change in the wake of landslides triggered by the 14 April 2010 Yushu Earthquake of China. *Arabian J Geosci*. 7:2129–2138.
- Xu C, Xu X, Yao X, Dai F. 2013b. Three (nearly) complete inventories of landslides triggered by the May 12, 2008 Wenchuan mw 7.9 earthquake of China and their spatial distribution statistical analysis. *Landslides*. 11:441–461.
- Yalcin A, Reis S, Aydinoglu AC, Yomralioglu T. 2011. A GIS-based comparative study of frequency ratio, analytical hierarchy process, bivariate statistics and logistics regression methods for landslide susceptibility mapping in Trabzon, ne Turkey. *Catena*. 85:274–287.
- Yao X, Tham LG, Dai FC. 2008. Landslide susceptibility mapping based on support vector machine: a case study on natural slopes of Hong Kong, China. *Geomorphology*. 101:572–582.
- Yeon Y K, Han JG, Ryu KH. 2010. Landslide susceptibility mapping in Injae, Korea, using a decision tree. *Eng Geol*. 116:274–283.

- Yilmaz I. 2010. Comparison of landslide susceptibility mapping methodologies for Koyulhisar, Turkey: conditional probability, logistic regression, artificial neural networks, and support vector machine. *Environ Earth Sci.* 61:821–836.
- Yin Y. 2014. Vertical acceleration effect on landslides triggered by the Wenchuan earthquake, China. *Environ Earth Sci.* 71:4703–4714.
- Youssef AM, Pradhan B, Jebur MN, El-Harbi HM. 2014. Landslide susceptibility mapping using ensemble bivariate and multivariate statistical models in Fayfa Area, Saudi Arabia. *Environ Earth Sci.* 73:3745–3761.
- Youssef AM, Pourghasemi HR, Pourtaghi ZS, Al-Katheeri MM. 2015. Landslide susceptibility mapping using random forest, boosted regression tree, classification and regression tree, and general linear models and comparison of their performance at Wadi Tayyah basin, Asir Region, Saudi Arabia. *Landslides*. DOI: 10.1007/s10346-015-0614-1.
- Zhao W, Huang R, Ju N, Zhao J. 2014. Assessment model for earthquake-triggered landslides based on quantification theory I: case study of Jushui river basin in Sichuan, China. *Nat Hazards.* 70:1–18.
- Zhuang JQ, Javed I, Peng JB, Liu TM. 2014. Probability prediction model for landslide occurrences in Xi'an, Shaanxi Province, China. *J Mountain Sci.* 11:345–359.